Contrib Mineral Petrol (2014) 168:1051
DOI 10.1007/s00410-014-1051-1

ORIGINAL PAPER

Experimental constraints on rhyolite-MELTS and the Late Bishop Tuff magma body

James E. Gardner · Kenneth S. Befus · Guilherme A. R. Gualda · Mark S. Ghiorso

Received: 10 June 2013 / Accepted: 30 July 2014 / Published online: 13 August 2014

Abstract Thermodynamic models are vital tools to evaluate magma crystallization and storage conditions. Before their results can be used independently, however, they must be verified with controlled experimental data. Here, we use a set of hydrothermal experiments on the Late-erupted Bishop Tuff (LBT) magma to evaluate the rhyolite-MELTS thermodynamic model, a modified calibration of the original MELTS model optimized for crystallization of silicic magmas. Experimental results that are well captured by rhyolite-MELTS include a relatively narrow temperature range separating the crystallization of the first felsic mineral and the onset of the ternary minimum (quartz plus two feldspars), and extensive crystallization over a narrow temperature range once the ternary minimum is reached. The model overestimates temperatures by ~40 °C, a known limitation of rhyolite-MELTS. At pressures below 110 MPa, model and experiments differ in the first felsic phase, suggesting that caution should be exercised when applying the model to very low pressures. Our results indicate that for quartz, sanidine, plagioclase, magnetite, and ilmenite to crystallize in equilibrium from LBT magma, magma must have been stored at $\leq$740 °C, even when a substantial amount of CO_2 occurs in the coexisting fluid. Such temperatures are in conflict with the hotter temperatures retrieved from magnetite–ilmenite compositions (~785 °C for the sample used in the experiments). Consistent with other recent studies, we suggest that the Fe–Ti oxide phases in the Late Bishop Tuff magma body are not in equilibrium with the other minerals and thus the retrieved temperature and oxygen fugacity do not reflect pre-eruptive storage conditions.

Keywords Rhyolite · Thermodynamic model · Explosive eruptions · Experimental petrology

Communicated by G. Moore.

Electronic supplementary material The online version of this article (doi:10.1007/s00410-014-1051-1) contains supplementary material, which is available to authorized users.

J. E. Gardner (✉) · K. S. Befus
Department of Geological Sciences, Jackson School of Geosciences, The University of Texas at Austin, EPS Building Rm # 1.130 C9000, Austin, TX 78705, USA
e-mail: gardner@jsg.utexas.edu

G. A. R. Gualda
Earth and Environmental Sciences, Vanderbilt University, Nashville, TN 37235-1805, USA

M. S. Ghiorso
OFM Research–West, 7336 24th Avenue NE, Seattle, WA 98115, USA

Introduction

Immense eruptions of hundreds to thousands of cubic kilometers of magma are potentially the most hazardous events that face the planet, by injecting vast quantities of gas and ash into the atmosphere and covering 1000s of square kilometers with thick pyroclastic flows (Christiansen 2001; Rampino 2002; Baines and Sparks 2005; Self 2006; Wilson 2008; Self and Blake 2008). No eruption of that scale has happened in recorded history, and so our knowledge of such eruptions and of the magma bodies that give rise to them is entirely derived from existing deposits. It is thus of critical importance to understand where and under what conditions do large volumes of magma collect and differentiate in the crust.

Thermodynamic models are one way to evaluate the conditions under which magma collects and differentiates.

One such model is rhyolite-MELTS, a modified calibration of the original MELTS model that better captures the quartz-feldspar saturation surface, thus resulting in much better results for calculations relevant for silicic magmas (Gualda et al. 2012). It should be emphasized that the original calibration of MELTS had to be performed using very limited experimental data on silicic compositions; in particular, the only experimental dataset available was that of Naney (1983), with a granite of rhyodacitic composition being the most silicic Fe–Mg-bearing sample used in that study. Gualda et al. (2012) argue that the lack of relevant experimental data largely persists, with the few new relevant experimental datasets being plagued by shortcomings. They then use the average of early-erupted Bishop Tuff (EBT) glass inclusion compositions presented by Anderson et al. (2000)—which are very similar to the EBT average bulk pumice composition of Hildreth (1979), showing the "eutectoid" nature of EBT magma—as a constraint for the location of the ternary minimum. Gualda et al. (2012) show that the rhyolite-MELTS calibration is much superior, not only for the Bishop Tuff composition used, but also for available experiments and a few number of other natural systems they studied in greater detail, despite some discrepancies and inconsistencies (e.g., temperatures tend to be overestimated, agreement between observed and calculated sanidine compositions is relatively poor, and the sequence of crystallization for one of the studied compositions does not match expectations based on petrography). In this sense, a direct comparison of rhyolite-MELTS calculations with results from experiments specifically designed to test the calibration is of significant interest.

To evaluate the rhyolite-MELTS calibration, we have carried out an experimental phase equilibrium study using a pumice clast from the Late-erupted Bishop Tuff (LBT). The sample used is slightly less evolved than the reference EBT composition used for calibration of rhyolite-MELTS, but it still corresponds to a high-silica rhyolite and, as such, represents a good test of rhyolite-MELTS. Further, the Fe–Ti oxides in the sample used to record some of the highest crystallization temperatures (>780 °C) for the Bishop Tuff (see Hildreth 1979; Hildreth and Wilson 2007); it has recently been suggested that such temperatures do not represent pre-eruptive storage conditions (Ghiorso and Gualda 2013; see also Ghiorso and Evans 2008), putting into question the viability of the presumed stable vertical stratification of the Bishop Tuff magma body (Gualda and Ghiorso 2013), as initially proposed by Hildreth (1979; see also Hildreth and Wilson 2007). As such, experimentally constraining the appropriate crystallization temperature for this high-silica composition provides important new data on the structure and evolution of the Bishop Tuff, in particular, and the crystallization conditions of silicic magma bodies, in general.

Methods

The sample used in all experiments (AB-6202; see Pamukcu et al. 2012) was collected from the Ig2NW lobe, which forms part of the Late-erupted Bishop Tuff (Wilson and Hildreth 1997). AB-6202 is large, pinkish pumice that consists of vesicular glass and phenocrysts of quartz, sanidine, plagioclase, clinopyroxene, orthopyroxene, biotite, magnetite, and ilmenite (Table 1). Parts of AB-6202 were crushed to a coarse powder (<100 μm) to use in experiments; other parts were used to make mineral separates and thin sections for petrographic work. A grain mount of Fe–Ti oxides was made, and 22 ilmenites and 36 magnetites analyzed. No pair of grains was found in contact, but all crystals had adhering glass, and was thus in contact with the silicate melt. We combine the 58 mineral analyses to form 792 ilmenite–magnetite pairs, all of which passed the equilibrium test of Bacon and Hirschmann (1988). Together

Table 1 Composition of Late-erupted Bishop Tuff sample (AB-6202) used in this study

Phase	SiO_2	TiO_2	Al_2O_3	FeO*	MnO	MgO	CaO	Na_2O	K_2O	P_2O_5	*n*
WR	76.01	0.189	12.79	1.08	0.023	0.20	0.81	3.38	5.48	0.035	–
Glass	77.90 (71)	0.13 (4)	12.27 (16)	0.54 (20)	0.02 (1)	0.08 (1)	0.19 (3)	3.70 (15)	5.17 (7)	–	6
Sanidine	65.55 (96)	–	19.02 (22)	0.11 (4)	–	–	0.32 (8)	3.83 (19)	10.78 (48)	–	13
Plagioclase	62.59 (180)	–	23.66 (103)	0.21 (4)	–	–	5.29 (103)	7.94 (48)	1.13 (23)	–	32
Opx	51.90 (58)	0.11 (6)	0.40 (24)	27.30 (159)	1.15 (17)	18.40 (95)	1.01 (6)	–	–	–	14
Cpx	52.37 (4)	0.19 (0)	0.63 (15)	12.34 (83)	0.69 (9)	12.57 (57)	20.92 (6)	0.40 (1)	–	–	1
Magnetite	0.02 (2)	46.04 (80)	0.10 (2)	50.48 (156)	0.85 (15)	1.73 (18)	–	–	–	–	22
Ilmenite	0.07 (2)	8.35 (78)	1.22 (18)	85.02 (121)	0.50 (7)	0.80 (11)	–	–	–	–	35

All oxides are given in weight percent and averages of *n* number of grains. Total iron is reported as FeO. Whole-rock analysis by X-ray fluorescence; all other data by electron microprobe. Values in parentheses represent estimated standard deviations in terms of least units cited, thus 65.55 (96) indicates a standard deviation of 0.96 wt%. Matrix glass is reported normalized to 100 % (original total = 97.90)

WR whole rock, *Opx* orthopyroxene, *Cpx* clinopyroxene

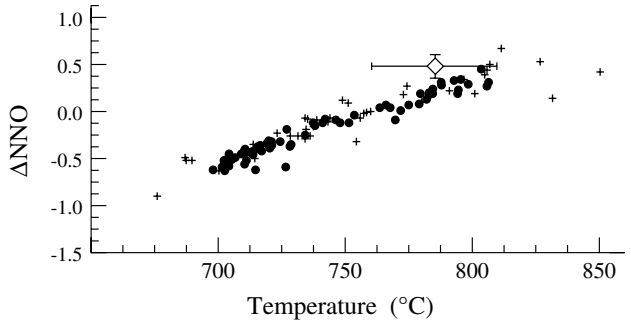

Fig. 1 Temperature and relative oxygen fugacity estimated from magnetite and ilmenite compositions in AB-6202 (Table 1), calculated using the model of Ghiorso and Evans (2008). Also shown is the full range of magnetite-ilmenite pairs from the Bishop Tuff, modified from Ghiorso and Evans (2008). *Black symbols* calculated from model of Ghiorso and Evans (2008); *solid circles* are data from Hildreth (1977); and *crosses* are data from Hildreth and Wilson (2007)

those compositions indicate a temperature of 783 ± 23 °C and an oxygen fugacity equal to 0.5 ± 0.1 log units above the Ni–NiO buffer (Fig. 1).

All experiments consisted of sample material plus distilled water held inside 3-mm OD Au capsules run in externally heated, cold-seal pressure vessels, made of a nickel-based alloy (Table 2). In all cases, enough water was added to the charge to ensure that the sample was water-saturated at run conditions. Reversal experiments consisted of aliquots of previously run material that were then run either at a hotter temperature and/or higher water pressure to induce melting or at a lower temperature and/or lower water pressure to induce crystallization. Pressure was measured to ± 0.1 MPa, and the K-type thermocouples used have been found to be precise to ±5 °C. The use of a Ni filler rod in the pressure vessel ensured that the sample hydrated at an oxygen fugacity slightly above that of the Ni–NiO oxygen buffer (Gardner et al. 1995). After 5–26 days, samples were quenched by removing their pressure vessel from the furnace and first blowing on the vessel with compressed air until it stopped glowing red and then immersing it in water.

Three additional "mixed volatile" experiments (Table 3) were run; each consisted of sample material in a 2-mm OD.

Table 2 Conditions and results of water-saturated experiments

Run	Start[a]	P[a] (MPa)	T[a] (°C)	Time (hrs)	$[H_2O]$[b] (wt%)	Products[c]
G-1188	Powder	175	800	118	5.61 ± 0.27	g
G-1189	Powder	100	800	118	4.48 ± 0.27	g, cpx
G-1190	G-1189	100	775	115	4.65 ± 0.11	g, cpx, mt
G-1192	G-1189	100	750	317	n.d.	–[c]
G-1193	Powder	175	800	185	n.d.	g
G-1194	G-1193	175	760	185	n.d.	g, cpx, bt
G-1196	Powder	100	700	216	n.d.	px, kf, pg, qtz, ox
G-1197	G-1190	100	740	362	n.d.	g, cpx, kf, mt
G-1198	G-1196	100	765	362	n.d.	g, px, ox
G-1199	G-1189	50	800	362	2.79 ± 0.25	g, px, kf, ox
G-1201	G-1188	175	760	173	n.d.	–[c]
G-1202	G-1196	175	740	337	n.d.	g, cpx, bt
G-1203	G-1201	175	720	337	n.d.	g, cpx, kf, ilm, bt
G-1206	Powder	100	750	362	n.d.	g, cpx, kf, ox
G-1215	G-1196	140	730	336	n.d.	g, px, ox
G-1216	G-1206	125	720	337	n.d.	g, px, kf, qtz, ilm, mt
G-1217	powder	175	730	336	n.d.	g, px, bt
G-1219	G-1206	100	720	621	n.d.	g, cpx, kf, qtz, pg, ilm, mt
G-1220	G-1216	125	700	616	n.d.	g, cpx, kf, pg, qtz, ilm, mt
G-1221	G-1217	175	710	616	n.d.	g, px, kf, bt, ox
G-1224	Powder	140	740	333	n.d.	g, px, bt
G-1225	Powder	150	700	501	n.d.	g, cpx, kf, pg, qtz, ox
G-1227	G-1224	140	715	331	n.d.	g, px, bt, kf, qtz, ox
G-1229	G-1224	125	735	351	n.d.	g, px, kf, bt
G-1230	Powder	200	700	351	n.d.	g, cpx, kf, bt, mt, ilm
G-1240	G-1192	50	760	409	n.d.	g, px, kf, qtz, mt, ilm
G-1241	G-1189	50	780	359	n.d.	g, px, kf, mt
G-1360	G-1188	75	800	262	3.61 ± 0.03	g, px, kf, ox

[a] Starting material was powder of AB-6202 or an aliquot of a previous run. *P* pressure, *T* temperature

[b] H_2O contents dissolved in glass as measured by FTIR, with estimated standard deviations listed. *n.d.* not determined

[c] Products: water bubbles present in all runs; *g* glass, *px* pyroxene [*cpx* = augite]; *kf* sanidine, *pg* plagioclase, *qtz* quartz, *bt* biotite, *ox* FeTi oxide [*ilm* = ilmenite, *mt* = magnetite]. Compositions are listed in Supplemental Appendix

[d] Not analyzed, used as starting material

Au capsule was welded on one end and crimped shut at the other. That small capsule was then placed inside a 5-mm OD Au capsule, along with distilled water and oxalic acid. Enough of each was added to ensure that a fluid phase was present during the experiment. All three experiments were run using the same techniques as the water-saturated experiments described above.

All capsules were removed from their pressure vessels and weighed to check that no leaks occurred during the experiment. The capsule was then cracked open. If fluid is present, a slight hiss can be heard when the capsule is broken. Only samples that did not leak and clearly had excess fluid present are included in this study. Samples were then sectioned for petrographic examination and analyzed with the electron microprobe and scanning electron microprobe (compositions of experimental products are given in the Supplemental Appendix). Magnetite, ilmenite, and pyroxenes were analyzed with a 10-nA beam current, 15 keV accelerating voltage, and a focused beam. Feldspars and glasses were analyzed using a 10-nA beam current, 15-keV accelerating voltage, and a defocused beam (2 and 10 μm diameter, respectively) to minimize Na migration. Na migration was monitored and corrected using the Na migration capability of probe for windows during glass analyses. Working standards were analyzed repeatedly to monitor for analytical quality and instrument drift during each microprobe session.

Dissolved H_2O and CO_2 contents in a few experimental glasses were analyzed by Fourier transform infrared (FTIR) spectroscopy, using a Thermo Electron Nicolet 6700 spectrometer and Continuμm IR microscope (Tables 2, 3). Three to six spectra were collected in transmittance mode at widely spaced positions in each glass, with each spectrum consisting of 60 scans at a resolution of 4 cm^{-1}. Dissolved CO_2 was measured in the mid-IR region (4,000–650 cm^{-1}) using an infrared light source and a KBr beamsplitter; dissolved H_2O was measured in near-IR (7,800–4,000 cm^{-1}) using white light and a CaF_2 beamsplitter. Contents of H_2O are sums of molecular (H_2O_m) and hydroxyl (OH) H_2O determined from absorbance at ~5,250 and ~4,500 cm^{-1}, respectively, using the model of Zhang et al. (1997). CO_2 contents were determined from absorbance at ~2,350 cm^{-1}, using a molar absorptivity value of 1,214 L mol^{-1} cm^{-1} (Behrens et al. 2004). The thickness where each spectrum was collected was measured optically using a petrographic microscope by focusing on the top and bottom of the sample and measuring the depth with a focus drive linear encoder attached to the microscope.

Results

In water-saturated experiments, only crystals and bubbles exist at 700 °C and 100 MPa, whereas only glass and bubbles exist at 800 °C and 175 MPa (Table 2). In between, glass and bubbles coexist with one or more mineral phases. The presence of gas bubbles in all run products attests to all being fluid saturated. Stable minerals are identified by their euhedral shape and/or as new rims on preexisting crystals. Anhedral crystals or those that exist only as cores are considered relicts that were unstable at run conditions. Only stable phases are reported (Table 2).

All experiments below 800 °C and 175 MPa contain clinopyroxene (Fig. 2). At 175 MPa, clinopyroxene and biotite become stable between 760 and 800 °C. We assume that clinopyroxene crystallized at higher temperature than biotite, because it is more abundant. Sanidine and ilmenite join the assemblage below 730 °C, and magnetite appears below 720 °C. Quartz and plagioclase are assumed stable below 710 °C. At 100 MPa, the crystallization sequence is clinopyroxene (>800 °C), magnetite (775–800 °C), sanidine (<760 °C), quartz plus ilmenite (<740 °C), and finally plagioclase. At 50 MPa, sanidine and magnetite grew at >800 °C. Ilmenite and quartz grew at 760 °C, with quartz occurring in granophyric intergrowths with sanidine. The solidus occurs between 700 and 720 °C. Biotite was not recognized at 100 MPa. Increasing water pressure thus suppresses the stabilities of anhydrous minerals, expands the stability of biotite, and stabilizes ilmenite at higher temperature relative to magnetite.

Matrix glass changes in composition systematically with temperature (Fig. 3). Concentrations of SiO_2 increase with decreasing temperature, whereas Al_2O_3, K_2O, and FeO contents decrease. At a given temperature, SiO_2 concentrations

Table 3 Conditions and results of mixed volatile experiments

Run[a]	Pressure (MPa)	Temperature (°C)	Time (h)	$[H_2O]$[b] (wt%)	$[CO_2]$[b] (ppm)	Products[c]
G-1350	200	785	237	4.13 ± 0.13	568 ± 41	g, px
G-1351	200	785	237	3.91 ± 0.23	701 ± 52	g, px, kf, ox
G-1359	250	785	361	4.94 ± 0.18	460 ± 19	g, px

[a] Starting material for all runs was powder of AB-6202

[b] H_2O and CO_2 contents dissolved in glass as measured by FTIR, with estimated standard deviations listed

[c] Products: water bubbles present in all runs; *g* glass, *px* pyroxene, *kf* sanidine, *ox* FeTi oxide

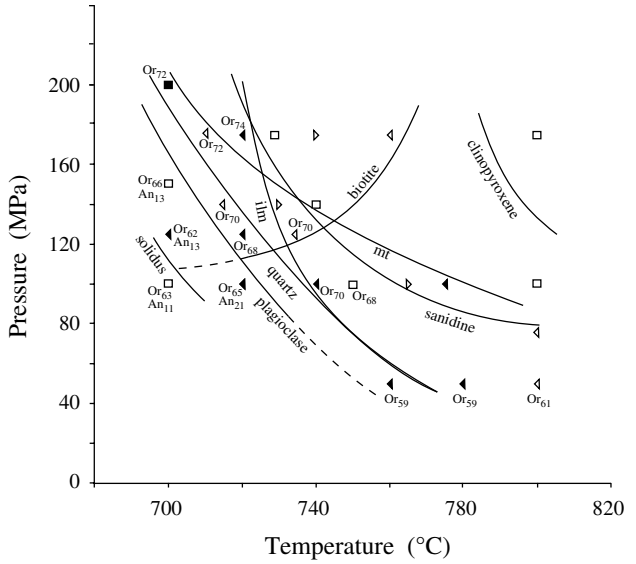

Fig. 2 Phase diagram for AB-6202, a sample of Late-erupted Bishop Tuff. *Curves* are upper stability limits for mineral phases and the location of the solidus. The stability *curves* for clinopyroxene and biotite at high temperatures are approximations. Average compositions of feldspars [orthoclase component (*Or*) for sanidine or anorthite component (*An*) in plagioclase] are shown next to the experiments in which they grew. The stabilities of magnetite (*mt*) and ilmenite (*ilm*) were delimited by analyzing ≥30 grains in nine experiments (*solid symbols*). *Squares* are experiments that used natural powder. Other runs used aliquots of previously run samples, producing either crystallization (*left pointing triangles*) or melting (*right pointing triangles*)

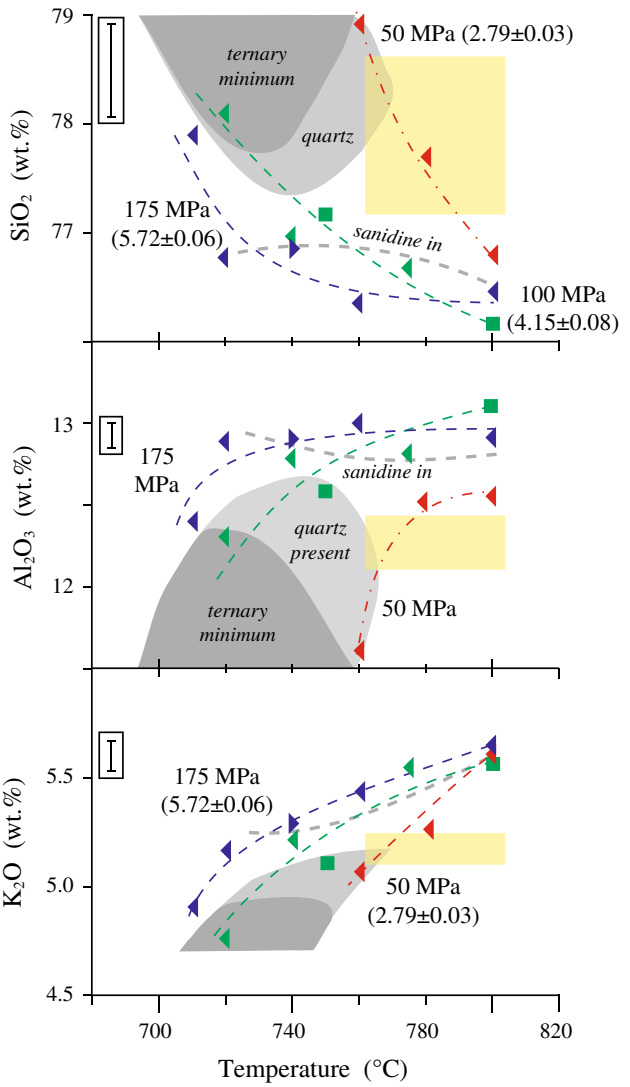

Fig. 3 Compositions of experimental glasses as a function of temperature for experiments run at 50 (*red*), 100 (*green*), or 175 (*blue*) MPa (see Fig. 2 for *symbols*). The average SD of the analyses is shown as an *error bar*. *Dashed lines* are approximate trends for visual impression and not regressions of the data. Conditions required for sanidine crystallization is shown as a *dashed gray line*. Those for quartz and the ternary minimum crystallization are outlined by *gray* fields. The average dissolved water contents of the experiments are listed, as estimated from the model of Liu et al. (2005). The error bars represent the spread in water content resulting from the nearly 100 °C range in temperature. The *yellow box outlines* the region defined by matrix glass composition (±1σ) and magnetite–ilmenite temperature (±1σ) for AB-6202

are greater at lower pressure, whereas Al_2O_3, K_2O, and FeO contents are greater at higher pressure. CaO and Na_2O concentrations are relatively constant with temperature and pressure. The abundance of glass was estimated and found to systematically decrease as temperature and pressure decrease (Fig. 4).

At all pressures, sanidine is stable at higher temperature relative to plagioclase and quartz (Fig. 2). Its composition ranges from Or_{61} to Or_{74}, and becomes more potassic as temperature and/or water pressure increases. Across the range of pressures, sanidine crystallization begins in melt with a similar composition (Fig. 3). The stability limit of quartz is well defined by its presence at 760 °C and 50 MPa, 720 °C and 125 MPa, and 715 °C at 140 MPa, and its absence at 740 °C and 100 MPa and at 700 °C at 200 MPa (Fig. 2). Plagioclase is stable at lower temperatures than quartz (Fig. 3). It varies in composition by ~10 mol% anorthite and generally becomes more sodic toward the solidus. Unlike sanidine, the melt that first precipitates quartz and plagioclase varies significantly in composition with pressure (Fig. 3).

The appearance of plagioclase coincides with significant changes in the experimental product. Samples with plagioclase are significantly more crystallized than those in which plagioclase is absent (Fig. 4). In addition, sanidine is usually more sodic when it coexists with plagioclase than when it does not (Fig. 2).

Mafic phases that crystallized are clinopyroxene, biotite, magnetite, and ilmenite (Fig. 2). Water pressure has no discernable impact on clinopyroxene composition, but lower temperature leads to clinopyroxene becoming more

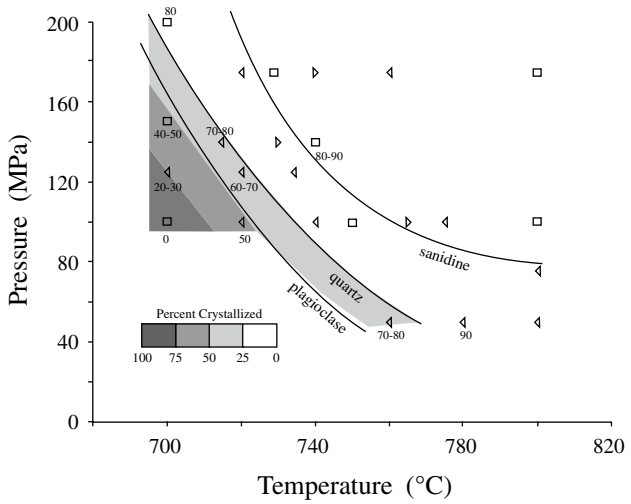

Fig. 4 Modified phase diagram showing the upper stabilities of the felsic minerals and estimated glass contents of various experiments. *Shaded regions* of the diagram delineate approximate variations in the amount of glass present. Samples are very rich in glass above the stability of quartz and decrease dramatically in glass content once plagioclase is present

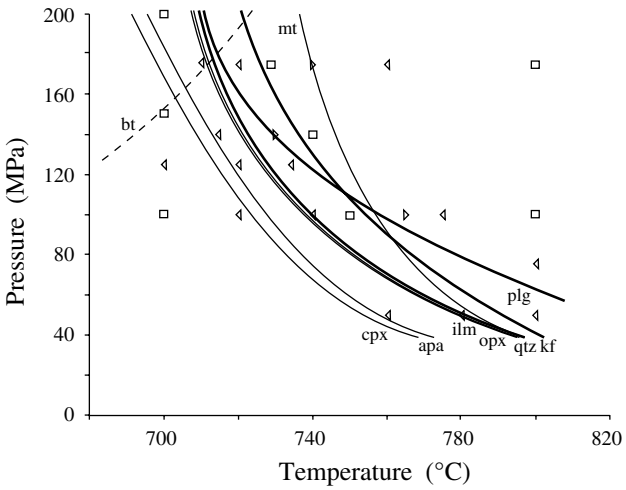

Fig. 5 Phase diagram for the Late-erupted Bishop Tuff (sample AB-6202), predicted by the rhyolite-MELTS model. Positions of experiments of this study are shown for reference. All stability *curves* have been decreased in temperature by 40 °C to approximate the experimental sanidine results (see Fig. 2). Stability *curves* for quartz (*qtz*), sanidine (*kf*), and plagioclase (*plg*) are shown in *bold*; other *curves* include clinopyroxene (*cpx*), apatite (*apa*), ilmenite (*ilm*), orthopyroxene (*opx*), magnetite (*mt*), and biotite (*bt*)

calcic (Wo component increases) and less magnesian (En decreases). The other mafic phases are too small to analyze quantitatively, but their presence was identified optically. In addition, nine experiments were examined using the scanning electron microscope to identify ilmenite and magnetite separately by collecting an EDS spectrum for each Fe–Ti oxide grain found. In cases where both are present, only 10–30 grains had to be measured before both were found. When only one was present, we analyzed more than 30 individual grains, and in some cases more than 70, to ensure that in fact only one was present. Magnetite is always more abundant when both are present and stable up to >800 °C at low pressures (Fig. 2). Between 100 and 200 MPa, ilmenite is not stable above 740 °C.

Discussion

The computational thermodynamics modeling package rhyolite-MELTS (Gualda et al. 2012) is a modification of MELTS (Ghiorso and Sack 1995) that is specifically optimized for the calculation of phase equilibria in quartz-bearing magmas. Our experimental results on bulk composition AB-6202 from the late-erupted Bishop Tuff can be compared to phase relations predicted by rhyolite-MELTS to assess the applicability of that model to high-silica rhyolites. A phase diagram for AB-6202 calculated from rhyolite-MELTS showing stability fields for sanidine, quartz, plagioclase, clinopyroxene, orthopyroxene, biotite, magnetite, ilmenite, and apatite is illustrated in Fig. 5. These estimated stability relations should be compared to the experimental phase diagram presented in Fig. 2. The first thing to note is that all of the experimentally determined phases are identified by the model. Additionally, the model predicts that the thermal stabilities of all phases are depressed with increasing water pressure, with the exception of biotite, a result that is consistent with the experimentally determined phase diagram (Fig. 2). A rigorous comparison of results presented in Figs. 2 and 5 reveals, however, a number of discrepancies that we discuss below.

Rhyolite-MELTS was optimized to replicate crystallization of quartz and the felsic minerals by making small adjustments to the calorimetrically determined enthalpy of formation of quartz and of the potassium end-member of alkali feldspar. The calibration was aimed at accurately locating the quartz + two-feldspar + fluid-saturated ternary minimum in high-silica rhyolite bulk compositions. Consequently, we focus first on comparing the relative stabilities of quartz and the feldspars between experiments and model.

Experimentally, sanidine is the first felsic mineral to crystallize at all pressures. In contrast, rhyolite-MELTS predicts that sanidine crystallizes first only above 110 MPa (Fig. 5). At lower pressures, the model predicts plagioclase to crystalize before sanidine, followed by quartz. Importantly, the modeled liquidus temperature for sanidine above 110 MPa is about 40 °C higher than observed; this temperature offset carries through to the onset of plagioclase and quartz saturation and is a recognized issue with

rhyolite-MELTS [Gualda et al. (2012) estimated that such phases appear on the liquidus some 30–40 °C higher than expected]. In terms of pressure, however, the modeled and experimental phase diagrams require no relative adjustment, and so in Fig. 5, we have lowered the modeled results by 40 °C in order to compare them directly to experiments. The need for this translation probably lies in the underlying model formulation for the entropy of the silicate liquid. If the modeled configurational entropy of the liquid is too small, then the liquid stability field relative to the solid phases will be shifted to higher temperatures than observed. Conversely, increasing the entropy of the liquid relative to the solid phases would expand the modeled liquid stability field, and better match the experimental observations. Importantly, as the experimental phase diagram is approximately recovered after temperature translation of the modeled phase relations, the entropy mismatch is not a function of liquid composition. To increase the modeled entropy of the liquid and bring both phase diagrams (Figs. 2, 5) into absolute agreement would require a reformulation of the configurational entropy to describe a more depolymerized liquid. This is a surprising and counterintuitive conclusion that clearly requires further experimental verification and insight in order to reformulate and recalibrate a liquid model with better thermometric fidelity. The immediate practical consequence of our experimental comparison to model results from rhyolite-MELTS is that the calculated phase diagram must be shifted down in temperature by 40 °C but shows no systematic offset in pressure.

We can further compare model predictions relative to experimental results by investigating differences in the upper temperature stability limits of quartz and plagioclase relative to sanidine (Fig. 6; the onset of sanidine crystallization is the zero point on the abscissa). The experimental results establish the upper temperature limits that clearly delineate the presence or absence of a phase at 50, 100, 125, 140, and 175 MPa. Quartz begins to crystallize at temperatures ≥30 °C colder that of sanidine at 50 MPa, but that range decreases to ~10–25 °C above 110 MPa. Plagioclase crystallizes at lower temperatures than quartz, but like quartz, its thermal stability increases relative to sanidine as pressure increases. In summary, the thermal gap between sanidine crystallization and the onset of the ternary minimum decreases from >50 °C at 50 MPa to ≥15 °C at 175 MPa (Fig. 6).

The rhyolite-MELTS model (Fig. 6) predicts that plagioclase is stable at temperatures ~15 °C above that of sanidine at pressures 50 MPa, and up to ~10 °C below sanidine at ~170 MPa. In contrast, the upper thermal stability of quartz is ~10–15 °C below that of sanidine at all pressures. In the model results, the thermal gap between crystallization of the first felsic mineral and the onset of the ternary minimum decreases from ~25 °C at 50 MPa to ~10 °C at

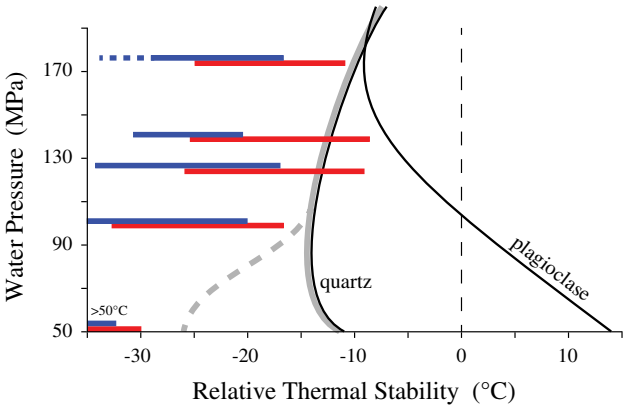

Fig. 6 Upper thermal stabilities of quartz and plagioclase relative to sanidine. Ranges for quartz (*red*) and plagioclase (*blue*) are shown based on reasonable allowable changes in the positions of their stabilities in pressure–temperature space at 50, 100, 125, 140, and 175 MPa (Fig. 1). The ranges do not take into account the ±5 °C error on the thermocouple. Relative thermal stability equals the highest temperature at which quartz or plagioclase crystallizes minus that for sanidine at a given pressure. Upper stability of plagioclase is more than 50 °C below that of sanidine at 50 MPa. *Black lines* show variations in thermal stabilities calculated using the rhyolite-MELTS model and the bulk composition of AB-6202. Note that below 110-MPa plagioclase is predicted to be stable at higher temperatures than sanidine

175 MPa (Fig. 6). On the whole, the modeled onset of the ternary minimum, *relative to the first appearance of sanidine*, is within 5–7 °C (over the range 100–180 MPa) of the experimental value; the intrinsic thermocouple error of the experiments is ~5 °C.

An important result of this experiment-model comparison is that the onset of the ternary minimum is captured well by the model (Fig. 6). Both experiments and model find that the temperature interval between crystallization of the first felsic mineral and the onset of the ternary minimum decreases as water pressure increases. Once the ternary minimum is reached, rhyolite-MELTS predicts that crystallization jumps from ~30 to ~70 % over a range of just a few degrees. We cannot resolve such small temperature differences experimentally, but we do find a significant increase in the amount of crystallization, from roughly 20–30 % just above the minimum to ≥50 % once quartz and both feldspars are stable (Fig. 4).

Experimental, modeled, and natural compositions (from Hildreth 1977) of feldspars are plotted in Fig. 7. For the natural compositions, all units in the Bishop Tuff, both early and late, are presented. Modeled feldspar compositions derived from the late-erupted pumice used as a starting material in this study are plotted as evolving compositional paths from high temperature to low temperature at three pressures, as indicated. The symbol along the evolution path indicates the temperature for the onset of quartz

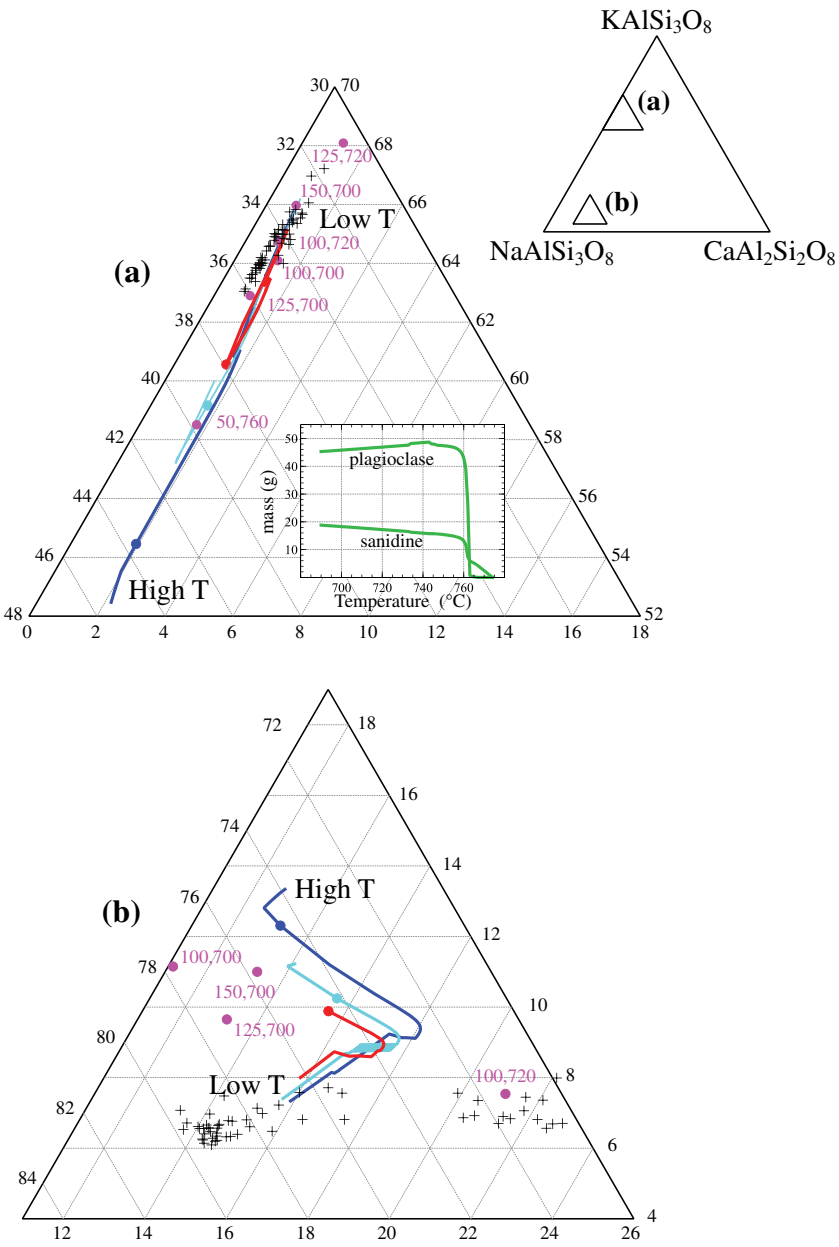

Fig. 7 Natural (Hildreth 1977), experimental (this study), and modeled (rhyolite-MELTS) feldspar compositions, plotted in portions of the $NaAlSi_3O_8$–$KAlSi_3O_8$–$CaAl_2Si_2O_8$ ternary. Experimental and modeled compositions are based on starting composition AB-6202. Natural compositions (*black crosses*) correspond to phenocrysts from all units in the Bishop Tuff. *Modeled curves* are drawn for continuous equilibrium temperature evolution (high to low as indicated) along three *isobars*: 190 MPa (*red*), 150 MPa (*cyan*), and 110 MPa (*blue*). Filed *magenta circles are* experimental run products labeled by tuples of pressure (MPa), temperature (°C). *Small diagram* on *top right* shows the positions of enlarged portions in the ternary. **a** Enlargement showing sanidine data. Note the reversal in evolution trend for the model run at 150 MPa. The *inset* shows the modeled mass of sanidine and plagioclase crystallizing as a function of temperature at 150 MPa. Observe the resorption of plagioclase which commences ~15 °C below the ternary minimum. **b** Enlargement showing plagioclase data. The *red-*, *cyan-*, and *blue-filled circles* indicate the onset of quartz saturation in the model runs

crystallization. Experimental run products are plotted and labeled by a *P*, *T* tuple in units of MPa and °C. All plotted experimental feldspar grew in the presence of quartz.

Figure 7a illustrates that there is broad coincidence between compositions of experimentally grown and naturally occurring sanidine. Modeled results better match both experiment and the rocks at pressures above 150 MPa. Experimentally, the composition of sanidine is more potassic (~Or_{70+}) above the ternary minimum and evolves to become more sodic (~Or_{65}) after the minimum is reached (Figs. 2, 7a). These experimental results confirm the expected trends deduced from analysis of the $CaAl_2Si_2O_8$–$NaAlSi_3O_8$–$KAlSi_3O_8$–SiO_2–H_2O phase diagram by Carmichael (1963, p 111). The model predicts that sanidine evolves continuously to more potassic compositions at low (50 MPa) and high (190 MPa) pressures (Fig. 7b). Sanidine exhibits a more complex composition evolution at 150 MPa, involving first enrichment in soda with decreasing temperature and then enrichment with potash, the reversal coincident with the ternary minimum. As discussed previously (Gualda et al. 2012), the modeled sanidines are more sodic then those observed in the LBT rocks, probably because of the systematic temperature offset discussed above.

Comparison between modeled plagioclase compositions, those grown experimentally, and those found in the Bishop deposits shows some systematic discrepancies (Fig. 7b). The modeled reversal in enrichment in lime exhibited at

all pressures is associated with resorption of plagioclase at temperatures below the ternary minimum (see temperature–mass inset in Fig. 7a); the resorption of plagioclase is expected for bulk compositions potassic enough to place sanidine first on the liquidus and then followed by quartz and plagioclase (Carmichael 1963). The offset between modeled plagioclase compositions and those found in nature could again result from the systematically high temperatures for phase relations predicted by rhyolite-MELTS.

Overall, the rhyolite-MELTS model reproduces to first order the crystallization sequence of our experimental results, particularly for pressures >100 MPa. Both experiments and model find that once the first felsic phase precipitates, the ternary minimum is reached upon cooling of only a few to a few 10s of degrees (Fig. 6). Onset of the ternary minimum then results in extensive crystallization over a narrow temperature range (Fig. 4). There are disparities in absolute temperatures, which felsic phase crystallizes first, and predicted feldspar compositions, which suggest that the model needs refining, but the narrow crystallization interval and the quartz–sanidine relations seem robust.

Modeled saturation surfaces for the minor phases (Fe–Ti oxides, pyroxenes, and biotite) poorly match the experimentally determined phase relations. As an example, at 160 MPa, clinopyroxene appears first on the liquidus at ~790 °C, followed by biotite at ~755 °C, then both ilmenite and magnetite at ~725 °C, a few degrees above the ternary minimum. In contrast, rhyolite-MELTS puts magnetite on the liquidus, with ilmenite and orthopyroxene appearing at the ternary minimum, and clinopyroxene and biotite appearing about 10 °C below that (Fig. 5). Experimentally, magnetite is stable at higher temperatures than the felsic minerals at low pressure, but less stable at high water pressures (Fig. 2); the model magnetite saturation curve has a steeper slope that results in an opposite trend (Fig. 5). The experimental stability fields for clinopyroxene and biotite are greatly expanded compared to those predicted. Finally, orthopyroxene is not stable experimentally, but it does form in the model, although only at near-solidus conditions; interestingly, LBT pumice contains orthopyroxene. There are many suggestive arguments that could explain these differences in minor phase stability relations. First and foremost is the observation that rhyolite-MELTS, and the original MELTS, contains little experimental data on which to base a calibration of the saturation surface of these minerals in highly silicic liquids, the principal source being the study of Naney (1983). While the thermodynamic properties of the mineral solid solutions are independently known and applicable to the compositions found in these rocks and experiments, the properties of the liquid state are poorly known, largely extrapolated from more mafic compositions, and have only been assessed for internal consistency with regard to the stability relations of quartz and the feldspars (Gualda et al. 2012). The second reason that the minor phases may differ between model and experiment is related to redox state. The experiments were configured to hold the redox state of the system to slightly above the NNO buffer. The model was also so constrained. It is possible that excursions from nominal NNO conditions could occur experimentally, which would in turn affect the Fe_2O_3/(FeO + Fe_2O_3) ratio in the melt, and could have a significant effect on the stability relations of all Fe-bearing minerals (Ghiorso and Evans, 2008). The third issue to consider is bulk composition. The model results are based on a chemical analysis of the experimental starting composition. The stability relations of pyroxenes, magnetite, ilmenite, and biotite depend quite critically on the magnesium content of this bulk composition, which is quite low (0.20 wt%; Table 1). The analysis for MgO is of course subject to uncertainty, and at these low concentrations, that error could easily be 50 %, causing the modeled stability fields to vary widely as a consequence. Of all these explanations, the most probable is the first, which suggests that improvements to rhyolite-MELTS must rely on expanding the database of well-characterized experimental phase relations in highly silicic magmas. The experimental data presented in this paper start that effort, but they are no means sufficient for a comprehensive recalibration of rhyolite-MELTS.

Implications for the Late Bishop Tuff magma body

Our experimental study used a sample of pumice from the late-erupted Bishop Tuff (LBT) as starting material. The LBT has traditionally been interpreted as derived from the hottest, least evolved, and deepest portions of a stratified magma body (Hildreth 1979; see also Hildreth and Wilson 2007). In contrast, Gualda and Ghiorso (2013) have recently suggested that the LBT constitutes a separate batch of magma that crystallized at similar temperatures and pressures to the EBT (the early-erupted Bishop Tuff), likely with no chemical exchange between the two bodies and no chemical or thermal stratification within either body. Using thermodynamic consistency, arguments related to titania activity Ghiorso and Gualda (2013) have shown that the Fe–Ti oxides are not in equilibrium in the Bishop magma, concluding that these oxides do not record pre-eruptive conditions (see also, Ghiorso and Evans 2008). Their arguments bring into question the deeper and hotter derivation of the LBT magma, which is a result inferred from two-oxide equilibria.

Phenocrysts in LBT pumice are distinctively zoned in trace elements. Quartz and zircon interiors are relatively poor in Ti, suggesting that they first grew in rhyolite at temperatures similar to those of the EBT (Wark et al. 2007; Reid et al. 2011). Outer rims of many quartz grains

are relatively bright in cathodoluminescence and rich in Ti, and those on sanidine are rich in Ba (Hervig and Dunbar 1992; Anderson et al. 2000; Peppard et al. 2001; Wark et al. 2007). In addition, glass inclusions in those rims are relatively enriched in CO_2 relative to inclusions in grain interiors (Anderson et al. 2000; Roberge et al. 2013), and all glass inclusions are more evolved in trace-element composition than their host matrix glasses (Roberge et al. 2013). These observations have been interpreted to suggest that the LBT underwent mixing with hotter, more mafic, magma just prior to eruption (Wark et al. 2007; Roberge et al. 2013). Anderson et al. (2000) pointed out, however, some difficulties in explaining the compositional variability in glass inclusions through mixing. Further, Zr contents in rim glass inclusions (see Peppard et al. 2001; Gualda and Ghiorso 2013) are relatively low and inconsistent with these high temperatures, particularly if the new calibration of Boehnke et al. (2013) is utilized. And, critically, on the basis of diffusion models of measured concentration profiles, Gualda and Ghiorso (2013) suggest that rim crystallization times are very short (months to a few years) and consistent with rim growth during eruptive decompression (see also Gualda 2007; Pamukcu et al. 2012); the timescale for mixing and homogenization of hotter magma into cooler, highly viscous rhyolite is far longer than can be accommodated by the diffusion time scales for rim growth.

Most of the LBT consists of rhyolite pumice with quartz, plagioclase, sanidine, biotite, clinopyroxene, orthopyroxene, magnetite, and ilmenite (Hildreth and Wilson 2007). It is important to note that if the Ti-rich rims on quartz and the Ba-rich rims on sanidine preserve a record of the mixing process, then those phases must have been stable and crystallizing in the magma after mixing (Evans and Bachmann 2013). If magnetite and ilmenite are assumed to be in equilibrium, as Hildreth and Wilson (2007) and Evans and Bachmann (2013) argue, then the elevated Ti contents in quartz rims can be interpreted as resulting from crystallization at temperatures that overlap with those obtained by magnetite–ilmenite geothermometry (Wark et al. 2007). It should be noted, however, that retrieving absolute temperatures from Ti in quartz is complicated, given the competing effects of temperature, titania activity, pressure (Thomas et al. 2010), and crystal growth rate (Huang and Audétat 2012). Temperatures derived from oxygen isotope exchange between quartz and magnetite also overlap those from magnetite–ilmenite geothermometry (Bindeman and Valley 2002). The implication of the two-oxide, oxygen isotope, and Ti-rim geothermometric assessment is that the LBT crystallized at high temperatures, with quartz, sanidine, magnetite, and ilmenite remaining stable above 750 °C and, possibly, higher than 800 °C (Fig. 1). All of those phases, and in addition plagioclase, are present as euhedral phenocrysts in AB-6202 (Table 1), as they are in most LBT samples (Hildreth 1977; Hildreth and Wilson 2007). We now demonstrate that the elevated temperatures deduced from the traditional geothermometry are inconsistent with our experimentally determined phase diagram and with other studies of phase stability relations in the Bishop magma.

Scaillet and Hildreth (2001) carried out an experimental study of the Bishop Tuff, using samples from both EBT (Ig1Ea) and LBT (Ig2NWb). All runs were water saturated at 200 MPa. For their LBT sample, plagioclase was the liquidus felsic mineral, at 775 °C, followed by alkali feldspar at 717 °C and then quartz at ~710 °C. The appearance of alkali feldspar in those experiments matches almost exactly where it appears in our runs, based on our results at 175 MPa, and the appearance of quartz differs by only ~10–15 °C (Fig. 2). In contrast, the plagioclase stability field differs substantially, appearing at ~775 °C (Scaillet and Hildreth 2001) versus <700 °C (this study). As the Scaillet and Hildreth (2001) study is available only in abstract form, we have no way to critically assess the origin of this discrepancy, other than to speculate that it lies in their using a starting composition containing higher CaO and lower SiO_2 than ours (see below). Biotite and clinopyroxene are stable over the entire temperature range explored by Scaillet and Hildreth (2001), in good agreement with our results. They found Fe–Ti oxides stable across the whole range of temperatures studied; we found these phases coexist only below 730 °C. Neither study crystallized orthopyroxene under any condition, despite its common presence in LBT magma.

There are important differences in bulk composition between the LBT samples used in Scaillet and Hildreth's (2001) experiments (e.g., SiO_2 content = 72.6 wt%) and our study (e.g., SiO_2 content = 76.0 wt%). Those differences probably account for the majority of discrepancies between the two sets of experiments, particularly the crystallization of plagioclase at much higher temperatures in the experiments of Scaillet and Hildreth (2001). Regardless of these differences, however, the important conclusion to draw from the Scaillet and Hildreth (2001) study is that it corroborates our result in establishing that the equilibrium ternary minimum assemblage—quartz, plagioclase, sanidine, vapor—is stable at 200 MPa and water-saturated conditions *only* at temperatures below 710 °C. Unfortunately, the Scaillet and Hildreth (2001) study is limited to only one pressure condition. Our experimental results can be used to interpret intensive variable conditions in the LBT for a variety of pressures and more general conditions of water undersaturation.

In order to compare our experimental results to the LBT, we re-plot phase relations in terms of dissolved water content (Fig. 8). We did not measure water contents in all of the experiments, because many are relatively crystal rich,

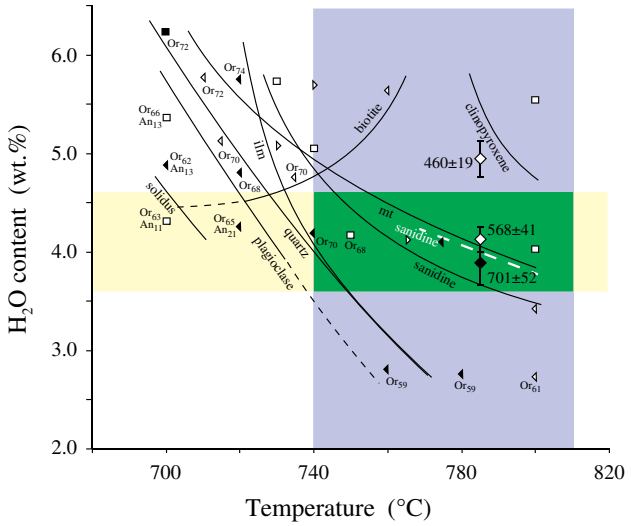

Fig. 8 Phase relations for AB-6202 with variations in temperature and dissolved H_2O contents. See Fig. 2 for *symbols* and *curves*. Dissolved H_2O contents were estimated from the model of Liu et al. (2005). In addition, three mixed volatile experiments are shown (see Table 3) as *diamonds* and *plotted* at their H_2O contents as measured by FTIR. The dissolved CO_2 contents ($\pm 1\sigma$) are listed next to the experiments. Sanidine and magnetite are found in the experiment plotted as the filled diamond; clinopyroxene only is found in the experiments *plotted* as *open diamonds*. The upper stability of sanidine is thus raised (*dashed line*), whereas the stability of magnetite is unaffected. More than 90 % of all LBT samples have temperatures between 740 and 800 °C (Hildreth and Wilson 2007; Ghiorso and Evans 2008), outlined by the *blue box*, whereas the dissolved H_2O content in late grown, Ti-rich quartz inclusions is ~3.6–4.6 wt% (Roberge et al. 2013), outlined by the *yellow box*. Most of the LBT magma body is thought to have equilibrated at conditions outlined by the overlap between temperatures and H_2O (*green box*)

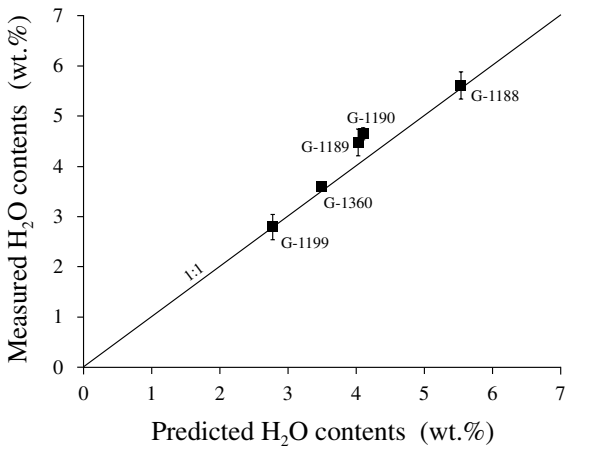

Fig. 9 Dissolved H_2O contents (in wt%) measured in five water-saturated experiments as a function of dissolved H_2O contents predicted by the model of Liu et al. (2005) at the temperature and pressure of the experiment. See Table 2 for data

making FTIR measurements difficult. Instead, we estimate water contents from the water solubility model of Liu et al. (2005), which reproduces dissolved water contents in high-silica rhyolite melts well (Gardner 2009; Gualda et al. 2012). As a check, we measured dissolved H_2O contents in five run products (Table 2) and find good agreement between measured and model contents across the range of water pressures (Fig. 9).

Glass inclusions in quartz from LBT mostly contain 3.8–5 wt% water (Wallace et al. 1999; Roberge et al. 2013). In addition, they contain ~100–800-ppm dissolved CO_2. Inclusions trapped within the outer, Ti-rich rims of quartz are richer in CO_2 compared to those in Ti-poor interiors (Anderson et al. 2000). Inclusions in the Ti-rich rims have between ~3.6 and ~4.6 wt% water and ~550 to ~950 ppm CO_2. Assuming that the dissolved pre-eruptive water content in AB-6202 was ~3.6–4.6 wt%, and the ternary minimum occurs between ~720 and ~740 °C (Fig. 8). At temperatures above the first appearance of plagioclase, quartz and sanidine coexist only below ~750 °C. Clinopyroxene, magnetite, and ilmenite are stable at those conditions, but biotite would require slightly greater H_2O contents at those temperatures in order to grow. Overall, it appears that the LBT magma represented by AB-6202 must have been stored at <720–740 °C for quartz, sanidine, plagioclase, clinopyroxene, magnetite, ilmenite, and biotite to be crystallizing in equilibrium. The compositions of plagioclase and sanidine in AB-6202 are An_{20-25} and Or_{64}, respectively, which match those of experimental feldspars at the ternary minimum at ~4 wt% water and <740 °C (Fig. 8). In addition, the relatively evolved composition of matrix glass (the most abundant phase) in AB-6202 is consistent with crystallization below 740 °C (Fig. 3).

Most of our experiments were water saturated, with no dissolved CO_2. It could be argued that the elevated concentrations of CO_2 dissolved in the melt stabilized quartz, plagioclase, sanidine, ilmenite, and biotite at significantly higher temperatures (recall that Fe–Ti oxide temperature estimates from LBT samples reach ~850 °C; see Fig. 1), but it is unlikely that dissolved CO_2 contents of 0.05–0.09 wt% would impact mineral stabilities by 50–100 °C (Gualda and Ghiorso 2014). To check this assertion, we ran three experiments that equilibrated AB-6202 with a mixed volatile fluid at 785 °C (Table 3). The products of those runs generally match experimental results at water saturation, except that sanidine is stabilized at slightly higher water contents. Importantly, these data confirm that that quartz, sanidine, ilmenite, magnetite, plagioclase, biotite, clinopyroxene, and orthopyroxene could not crystallize together at 783 °C, and certainly not at >800 °C, assuming H_2O and CO_2 contents observed in the Ti-rich quartz rim inclusions.

It is relevant to this line of discussion to understand the origin of the displacement of the sanidine-in curve for the CO_2-bearing experiments shown in Fig. 8. The

experimental runs that suggest this 10 °C displacement contain between 560 and 700 ppm CO_2 in the liquid phase, making CO_2 a trace constituent. Its effect on the activities of dissolved major melt components (including H_2O) is consequently expected to be trivial, and certainly not the cause of the apparent offset to the phase boundary. The origin of this offset results, in fact, from the difference in total pressures between the CO_2-absent and CO_2-present runs. At equivalent water concentrations, two melts of roughly the same bulk composition will have equivalent water fugacities. If one melt contains trace quantities of CO_2 and is saturated with a mixed H_2O–CO_2 fluid phase, the total pressure over the system will be essentially the sum of the fugacities of both H_2O and CO_2, and as the fluid phase contains an appreciable concentration of CO_2, from the strong differential melt-fluid partitioning, the total pressure will be significantly higher for the CO_2-bearing experimental charges of equivalent bulk water contents. As a case in point, for the water-bearing experiments that define the sanidine-in curve at ~4 wt% dissolved water (Fig. 8), the total pressure is 100 MPa, whereas the mixed fluid-experiments that delineate the displacement of the sanidine-in curve at the same melt water contents are at 200 MPa. The important point is that the CO_2-bearing experiments plotted in Fig. 8 are at different total pressures than the CO_2-absent experiments, even though both have equivalent melt water contents. Hence, the mere presence of CO_2 in the liquid phase is not the origin of the temperature shift in the sanidine phase boundary. The shift results from the differences in pressure. At constant total pressure, the addition of trace amounts of CO_2 to the melt phase would have little measureable effect on the phase diagram.

Returning to the LBT, our results imply pre-eruptive storage of AB-6202 at 720–740 °C. This result conflicts with the 783 ± 23 °C calculated from magnetite and ilmenite compositions in AB-6202, and with essentially all temperatures estimated for LBT from magnetite–ilmenite geothermometry (Fig. 1), all of which exceed 740 °C and many in excess of 800 °C (Hildreth and Wilson 2007; Ghiorso and Evans 2008). Our results show, however, that at ~4 wt% dissolved water, Fe–Ti oxides cannot grow in equilibrium with quartz and two feldspars to record temperatures hotter than ~740 °C, even in the presence of a CO_2-rich fluid. As discussed above, Ghiorso and Gualda (2013) have concluded on independent grounds that the Fe–Ti oxides in the LBT deposits no longer preserve compositions from which pre-eruptive intensive variables can be deduced. We come to the same conclusion from the experimental results presented here. The most likely explanation for this result is that the Fe–Ti oxides did not grow in chemical communication with each other in the magma body or have had their magmatic compositions subsequently altered.

The conclusion that the Fe–Ti oxides are not in equilibrium is at odds with the conventional interpretation of the pre-eruptive state of the Bishop magma body. For example, Evans and Bachmann (2013) have recently argued that the Fe–Ti oxide minerals are in Fe^{2+}-Mg exchange equilibrium with each other and with coexisting biotite in the LBT, but not with pyroxene. They base this inference on the observation that ilmenite–magnetite and ilmenite–biotite compositions form quasi-linear relationships on Mg–Fe^{2+} Roozeboom plots (whereas ilmenite–pyroxenes pairs do not), concluding that the Fe–Ti oxide minerals and the biotite preserve magmatic Fe^{2+}–Mg ratios, and that Fe–Ti exchange two-oxide geothermometry may consequently be used to evaluate pre-eruptive conditions in the Bishop magma body. This deduction of Evans and Bachmann (2013) is problematic for two reasons. Firstly, the inferred Fe^{2+}/Mg ratio of the biotite more closely resembles a bimodal distribution rather than a linear correlation (Evans and Bachmann 2013, their Fig. 2; see also Gualda and Ghiorso 2013). This clustering is also the case for ilmenite and magnetite, as illustrated in Fig. 10. The bimodality can be correlated with the origin of the biotite, magnetite, and ilmenite from either the LBT or EBT eruptive units (Hildreth, 1977). Additionally, Evans and Bachmann (2013) assume Fe^{2+} contents in the biotite correspond to the total amount of iron as determined by microprobe analysis, whereas Hildreth (1977) demonstrated by independent wet chemical analysis of FeO in biotite that a significant proportion (40–80 %) of the iron in the biotites is oxidized.

Secondly, and more fundamentally, in correlating Fe^{2+}/Mg exchange between ilmenite and magnetite, Evans and

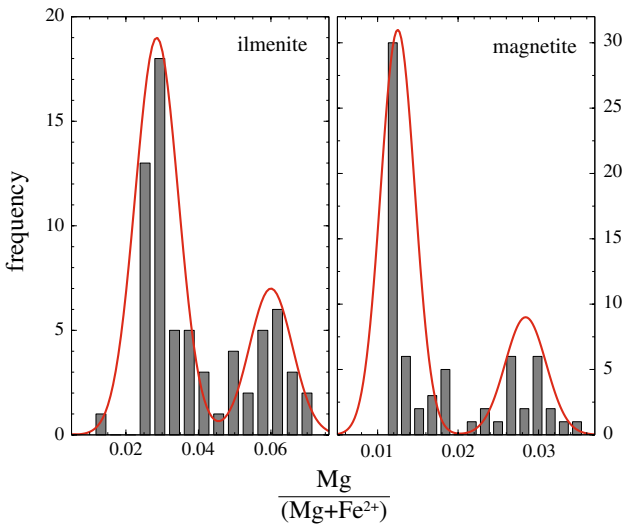

Fig. 10 Frequency *histograms* of molar Mg/(Mg + Fe^{2+}) ratios in ilmenite and magnetite calculated from reported compositions from the Bishop Tuff (Hildreth 1977). The *red curves* are best fit bimodal distributions optimized against the underlying *histograms*

Bachmann (2013) have not demonstrated that the chemical potential difference of the exchange reaction involving Fe^{2+} and Mg components for oxide pairs is zero over the inferred temperature range of interest. That is the requirement of exchange equilibrium. A simple correlation on a Fe^{2+}–Mg exchange plot between two phases does not imply thermodynamic exchange equilibrium, because the relation between composition ratio and activity ratio is not necessarily linear—and this is especially so for the Fe–Ti oxides (Ghiorso and Evans 2008). Even if the Fe–Ti oxide pairs are assumed to be in Fe–Mg exchange equilibrium, this result does not imply that the oxides are in Fe–Ti exchange equilibrium. In fact, Ghiorso and Evans (2008) have demonstrated that the ilmenite–magnetite pairs in the LBT cannot simultaneously be in Fe–Ti and in Fe^{2+}–Mg exchange equilibrium. They show that the assumption of Fe^{2+}–Mg exchange equilibrium between ilmenite–magnetite pairs in the LBT yields temperatures that vary randomly when compared to Fe–Ti exchange temperatures. Only at the lowest ilmenite–magnetite temperatures (~720 °C), do results derived from Fe–Ti exchange match those obtained from Fe–Mg exchange. Couple this observation with the analysis of Ghiorso and Gualda (2013), who show that the melt activity of titania that is inferred from ilmenite–magnetite pairs in the LBT generates a temperature-trend that is thermodynamically inconsistent and at odds with that inferred from the expected titania activity evolution of the melt phase, and the only permissible conclusion is that the Fe–Ti oxides no longer preserve Fe–Ti exchange equilibrium distributions. Whether or not these phases have Fe^{2+}/Mg ratios that wholly or partially preserve magmatic conditions is largely immaterial to the issue of the validity of Fe–Ti exchange geothermometry. Fe^{2+}–Mg exchange equilibrium, even if rigorously demonstrated with a proper thermodynamic analysis, is a necessary but not sufficient condition for establishing equilibrium between two or more phases. All possible exchange reactions must be in equilibrium for the phases to be in global equilibrium.

We conclude that temperature estimates from Fe–Ti oxides in the LBT are not reliable indicators of the growth conditions of phenocrysts in the magma body. Ignoring those, and instead focusing on equilibrium between sanidine, quartz, plagioclase, and rhyolitic melt that contains ~4 wt% H_2O and ~600 ppm CO_2, indicates that the LBT was stored at ~720–740 °C. This conclusion is in excellent agreement with the low (i.e., <750 °C) zircon saturation temperatures calculated by Gualda and Ghiorso (2013) for LBT using glass inclusion compositions from Wallace et al. (1999) and Anderson et al. (2000). Magnetite and ilmenite would crystalize at those temperatures and, in fact, compositions of a small minority of magnetite–ilmenite pairs in LBT predict such temperatures (Fig. 1). It is also those few pairs that suggest melt Titania activities that come closest to those implied by the glass compositions (Ghiorso and Gualda 2013). Clinopyroxene would also crystallize at 720–740 °C, but compositions of experimental clinopyroxene at those temperatures are distinctly more Fe-rich than those in LBT, which are invariant in composition despite the implied ~100 °C range in temperature (Hildreth 1977). Finally, as noted earlier, orthopyroxene does not crystalize in LBT samples (Scaillet and Hildreth 2001; this study), which is at odds with its ubiquitous presence in LBT. We cannot explain its absence, except to note that, just like clinopyroxene, the composition of orthopyroxene is invariant in the LBT (Hildreth 1977), which is nearly impossible if it crystallized over the ~100 °C range in temperature implied by the Fe–Ti oxides. The absence of orthopyroxene in the experiments and the mismatch in composition between natural and experimental clinopyroxene leads to the suggestion that both pyroxenes are out of equilibrium with the other phases in LBT; texturally, however, there is no indication of disequilibrium between pyroxenes and melt, so their origin remains elusive.

Conclusions

Experiments carried out on Late Bishop Tuff rhyolite indicate that the rhyolite-MELTS thermodynamic model can to first order reproduce the crystallization sequence of felsic phases, although rhyolite-MELTS overestimates absolute temperatures by ~40 °C. In particular, the narrow crystallization interval and the relationship of quartz-sanidine are robust. Given the predominance of felsic phases in rhyolite magmas, rhyolite-MELTS should be able to predict crystallization behavior of such magmas. On the other hand, the crystallization sequence of the mafic phases is poorly predicted, which most likely results from the limited experimental data for such phases in silicic melts used to calibrate the model.

The experimental phase relations demonstrate that the Late Bishop Tuff magma was stored at 720–740 °C, assuming the melt contained ~4 wt% H_2O. That result is at odds with the significantly hotter temperatures retrieved from magnetite–ilmenite compositions in Late Bishop Tuff rocks, including the sample used in this study. Those minerals are clearly not in equilibrium, when all possible exchange reactions are considered, and so we conclude that the temperature estimates derived from them are not reliable indicators of pre-eruptive magmatic conditions.

Acknowledgments We thank Ayla Pamukcu and Matt Williams for help with making mineral separates and scanning electron microprobe analyses. This project was partially funded by a Grant to J.E.G. from the US National Science Foundation (EAR-1049829). Critical reviews by Colin Wilson and an anonymous reviewer improved the manuscript.

References

Anderson AT, Davis AM, Lu FQ (2000) Evolution of Bishop Tuff rhyolitic magma based on melt and magnetite inclusions and zoned phenocrysts. J Petrol 41:449–473

Bacon CR, Hirschmann MM (1988) Mg/Mn partitioning as a test for equilibrium between coexisting Fe–Ti oxides. Am Mineral 73:57–61

Baines PG, Sparks RSJ (2005) Dynamics of giant volcanic ash clouds from supervolcanic eruptions. Geophys Res Lett 32:L24808

Behrens H, Tamic N, Holtz F (2004) Determination of the molar absorption coefficient for the infrared absorption band of CO_2 in rhyolitic glasses. Am Mineral 89:301–306

Bindeman IN, Valley JW (2002) Oxygen isotope study of the Long Valley magma system, California: isotope thermometry and convection in large silicic magma bodies. Contrib Mineral Petrol 144:185–205

Boehnke P, Watson EB, Trail D, Harrison TM, Schmitt AK (2013) Zircon saturation revisited. Chem Geol 351:324–334

Carmichael ISE (1963) The crystallization of feldspar in volcanic acid liquids. Quart J Geol Soc Lond 199:95–131

Christiansen RL (2001) The Quaternary and Pliocene Yellowstone plateau volcanic field of Wyoming, Idaho, and Montana. U.S. Geological Survey Professional Paper 729-G

Evans BW, Bachmann O (2013) Implications of equilibrium and disequilibrium among crystal phases in the Bishop Tuff. Am Mineral 98:271–274

Gardner JE (2009) The impact of pre-existing gas on the ascent of explosively erupted magma. Bull Volcanol 71:835–844

Gardner JE, Rutherford M, Carey S, Sigurdsson H (1995) Experimental constraints on pre-eruptive water contents and changing magma storage prior to explosive eruptions of Mount St. Helens volcano. Bull Volcanol 57:1–17

Ghiorso MS, Evans BW (2008) Thermodynamics of rhombohedral oxide solid solutions and a revision of the Fe-Ti two-oxide geothermometer and oxygen-barometer. Am J Sci 308:957–1039

Ghiorso MS, Gualda GAR (2013) A method for estimating the activity of Titania in magmatic liquids from the compositions of coexisting rhombohedral and cubic iron-titanium oxides. Contrib Mineral Petrol 165:73–81

Ghiorso MS, Sack RO (1995) Chemical mass transfer in magmatic processes IV. A revised and internally consistent thermodynamic model for the interpolation and extrapolation of liquid-solid equilibria in magmatic systems at elevated temperatures and pressures. Contrib Mineral Petrol 119:197–212

Gualda GAR (2007) Crystal and bubble populations in the early-erupted Bishop rhyolitic magma: Microscopy, X-ray tomography and microanalysis of pumice clasts. Dissertation, University of Chicago

Gualda GAR, Ghiorso M (2013) The Bishop Tuff giant magma body: an alternative to the Standard Model. Contrib Mineral Petrol 166:755–775

Gualda GAR, Ghiorso MS (2014) Phase-equilibrium geobarometers for silicic rocks based on rhyolite-MELTS. Part 1: principles, procedures, and evaluation of the method. Contrib Mineral Petrol 168:1033

Gualda GAR, Ghiorso MS, Lemons RV, Carley TL (2012) Rhyolite-MELTS: a modified calibration of MELTS optimized for silica-rich, fluid-bearing magmatic systems. J Petrol 53:875–890

Hervig RL, Dunbar NW (1992) Cause of chemical zoning in the Bishop (California) and Bandelier (New Mexico) magma chambers. Earth Planet Sci Lett 111:97–108

Hildreth EW (1977) The magma chamber of the Bishop Tuff: Gradients in temperature, pressure and compositions. Dissertation, University of California

Hildreth W (1979) The Bishop Tuff: evidence for the origin of compositional zonation in silicic magma chambers. Geol Soc Am Spec Pap 180:4–75

Hildreth W, Wilson CJN (2007) Compositional zoning of the Bishop Tuff. J Petrol 48:951–999

Huang R, Audétat A (2012) The titanium-in-quartz (TitaniQ) thermobarometer: a critical examination and re-calibration. Geochim Cosmochim Acta 84:75–89

Liu Y, Zhang Y, Behrens H (2005) Solubility of H_2O in rhyolitic melts at low pressures and a new empirical model for mixed H_2O–CO_2 solubility in rhyolitic melts. J Volcanol Geotherm Res 143:219–235

Naney MT (1983) Phase equilibria of rock-forming ferromagnesian silicates in granitic systems. Am J Sci 283:993–1033

Pamukcu AS, Gualda GAR, Anderson AT (2012) Crystallization stages of the Bishop Tuff magma body recorded in crystal textures in pumice clasts. J Petrol 53:589–609

Peppard BT, Steele IM, Davis AM, Wallace PJ, Anderson AT (2001) Zoned quartz phenocrysts form the rhyolitic Bishop Tuff. Am Mineral 86:1034–1052

Rampino MR (2002) Supereruptions as a threat to civilization on Earth-like planets. Icarus 156:562–569

Reid MR, Vazquez JA, Schmitt AK (2011) Zircon-scale insights into the history of a Supervolcano, Bishop Tuff, Long Valley, California, with implications for the Ti-in-zircon geothermometer. Contrib Mineral Petrol 161:293–311

Roberge J, Wallace PJ, Kent AJR (2013) Magmatic processes in the Bishop Tuff rhyolitic magma based on trace elements in melt inclusions and pumice matrix glass. Contrib Mineral Petrol 165:237–257

Scaillet B, Hildreth W (2001) Experimental constraints on the origin and evolution of the Bishop Tuff. In: Knesel K, Bergantz G, Davidson J (convenors) Geol Soc Am Penrose Conf: Longevity and dynamics of rhyolitic magma systems. Unpaginated volume of abstracts, 5 pp

Self S (2006) The effects and consequences of very large explosive volcanic eruptions. Philos Trans R Soc 364:2073–2097

Self S, Blake S (2008) Consequences of explosive supereruptions. Elements 4:41–46

Thomas JB, Watson EB, Spear FS, Shemella PT, Nayak SK, Lanzirotti A (2010) TitaniQ under pressure: the effect of pressure and temperature on the solubility of Ti in quartz. Contrib Mineral Petrol 160:743–759

Wallace PJ, Anderson AT, Davis AM (1999) Gradients in H_2O, CO_2, and exsolved gas in a large-volume silicic magma system: interpreting the record preserved in melt inclusions from the Bishop Tuff. J Geophy Res 104:20097–20122

Wark DA, Hildreth W, Spear FS, Cherniak DJ, Watson EB (2007) Pre-eruption recharge of the Bishop magma system. Geology 35:235–238

Wilson CJN (2008) Supereruptions and supervolcanoes: processes and products. Elements 4:29–34

Wilson CJN, Hildreth W (1997) The Bishop Tuff: new insights from eruptive stratigraphy. J Geol 105:407–439

Zhang Y, Belcher R, Ihinger PD, Wang L, Xu Z, Newman S (1997) New calibration of infrared measurement of dissolved water in rhyolitic glasses. Geochim Cosmochim Acta 61:3089–3100